
A discussion on the critical electric Rayleigh number for AC electrokinetic flow of binary fluids in divergent microchannel

Jin'an Pang(庞晋安), Yu Han(韩煜), Bo Sun(孙博), Wei Zhao(赵伟)[†]

State Key Laboratory of Photon-Technology in Western China Energy, International Collaborative Center on Photoelectric Technology and Nano Functional Materials, Laboratory of Optoelectronic Technology of Shaanxi Province, Institute of Photonics & Photon Technology, Northwest University, Xi'an 710127, China

ABSTRACT

Electrokinetic (EK) flow is a type of flow driven or manipulated by electric body forces, influenced by various factors such as electric field intensity, electric field form, frequency, electric permittivity/conductivity, fluid viscosity and etc. The diversity of dimensionless control parameters, such as the electric Rayleigh number, complicates the comparison of EK flow stability. Consequently, comparing the performance and cost of micromixers or reactors based on EK flow is challenging, posing an obstacle to their industrial and engineering applications. In this investigation, we theoretically derived a new electric Rayleigh number (Ra_e) that quantifies the relationship among electric body forces, fluid viscosity, and ion diffusivity, based on a tanh model of electric conductivity distribution. The calculation results indicate that the new Ra_e exhibits richer variation with the control parameters and better consistency with previous experimental reports. We further conducted experimental studies on the critical electric Rayleigh number (Ra_{ec}) of AC EK flow of binary fluids in a divergent microchannel. The experimental variations align well with the theoretical predictions, particularly the existence of an optimal AC frequency and electric conductivity ratio, demonstrating that the tanh model can better elucidate the underlying physics of EK flow. With the new electric Rayleigh number, we found that EK flow in the designed divergent microchannel has a much smaller Ra_{ec} than previously reported, indicating that EK flow is more unstable and thus more suitable for applications in micromixers or reactors in industry and engineering.

I. INTRODUCTION

Microfluidic device is a pivotal member of lab on a chip (LOC), facilitating the manipulation of fluids ranging from microliters to picoliters¹ in fields such as biomedical²⁻⁴ and chemical engineering,⁵⁻⁸ including applications like polymerase chain reaction (PCR)⁹, synthesis of nanoparticles¹⁰ and DNA sequencing chips.¹¹

Micromixer represents a significant category of microfluidic devices. According to the mechanism of mixing enhancement, micromixers are typically classified into two types: passive and active¹². Passive micromixers enhance mixing through the folding and stretching of fluids within specially designed microchannel geometries, requiring no additional driving mechanisms beyond a pressure gradient to induce flow disturbance.¹³⁻¹⁶ While passive micromixers often have specific functions, they generally lack versatility and exhibit relatively low mixing efficiency. In 2002, Stroock

et al.¹⁷ introduced a staggered herringbone mixer, discovering that at a Péclet number of 2×10^3 , the length required for 90% mixing was 7 mm, with the channel length needed for mixing increasing logarithmically with the Péclet number.

Active micromixers can significantly enhance mixing by applying external forces, such as electrostatic force,¹⁸ Lorentz force¹⁹ and acoustic pressure.²⁰ Electrokinetic (EK) micromixer is a specific type of active micromixer that enhances mixing by EK flow driven by electrostatic force, and experiences a rapid advancement since 1990s.²¹ In 1998, Baygents et al.²² investigated the neutral stability curves for EK flow under a DC electric field that parallel to the electric conductivity interface. In their investigation, the status of EK flow is characterized by an electric Rayleigh number (Ra_e , see Table I), which is determined by the electric intensity, the interface width and the gradient of electric conductivity. In

TABLE I. Definitions of Ra_e in different EK flow model. The red arrow indicates the flow direction, while the green arrow indicates the direction of the electric field.

Researchers	Baygents et al (1998) ²²	Chen et al (2005) ²³	Posner et al (2006) ²⁴	Wang et al (2014) ²⁵
Ra_e	$\frac{\varepsilon E^2}{D\mu} d^2 \frac{\Delta\sigma}{\sigma_1}$	$\frac{\varepsilon E^2}{4D\mu} \frac{dh^2}{\Delta y} \frac{(\lambda - 1)^2}{(\lambda + 1)^2}$	$\frac{\varepsilon E^2}{D\mu} h^2 \frac{\lambda - 1}{\lambda} \nabla^* \sigma^* \Big _{ma}$	$\frac{\varepsilon E^2}{D\mu} w^2 \frac{\Delta\sigma}{\sigma_1}$
Diagram of the EK flow				
Researchers	Wu et al (2015) ²⁶	Yoshikawa et al (2015) ²⁷	Hassen et al (2020) ²⁸	Nan et al (2022) ²¹
Ra_e	$\frac{\varepsilon E d}{K\mu}$	$\frac{e\Delta\theta l^3}{\mu\kappa} \nabla \frac{\varepsilon_{ref} E^2}{2}$	$\frac{\varepsilon E d}{K\mu}$	$\frac{4\varepsilon E^2}{D\mu} w^2 \frac{\lambda - 1}{\lambda + 1} (1 - \beta^2)$
Diagram of the EK flow				

E : Applied electric field; d : Channel width; σ_1 : Lower electric conductivity; σ_2 : Higher electric conductivity; $\Delta\sigma = \sigma_2 - \sigma_1$; D : Effective diffusivity; ε : Electric permittivity; μ : Dynamic viscosity; κ : Thermal diffusivity; Δy : Interface width; h : Channel height; $\lambda = \sigma_2/\sigma_1$: Electric conductivity ratio; K : Ionic mobility; b : Initial interface width; w : Initial width at the inlet; l : Characteristic length scale of the flow; θ : Temperature deviation; ε_{ref} : Electric permittivity at reference temperature; e : Coefficient; $\beta = 2\omega\varepsilon/(\sigma_1 + \sigma_0)$: Dimensionless number to evaluate the influence of frequency; $\nabla^* \sigma^*|_{max} \approx 1 - e^{-\left(\frac{b}{\Delta y}\right)^2} - e^{-\left(\frac{d-b}{\Delta y}\right)^2}$: Normalized maximum conductivity gradient;

2001, Oddy et al.²⁹ designed a delicate micromixer to promote mixing through EK instability induced by sinusoidal electroosmotic flow. Subsequently, Lin et al.³⁰ showed a plot of the growth rates of the most unstable eigenfunction in the wavenumber (k)— Ra_e space. They found the critical electric field required for mixing decreases as the electric conductivity ratio increases. In 2005, Chen et al.²³ defined a Ra_e (refer to Table I) for DC EK flow with electric conductivity difference in a T-shaped microchannel with a high aspect ratio. By experimental and analytical studies, they found the presence of both convective and absolute instabilities of EK flow. When the applied Ra_e is beyond a certain critical threshold, say $Ra_{ec} \approx 10$, the flow becomes convective unstable where the disturbance only grows downstream. When Ra_e is beyond a second $Ra_{ec} \approx 160$, the flow becomes absolute unstable, with the disturbances

propagating both upstream and downstream simultaneously. In 2006, Posner et al.³¹ studied the EK instability in a cross-shaped microchannel flow diagram. By defining a modified local electric Rayleigh number, characterized by the charge density as a function of the maximum electric conductivity gradients, they determined that the critical electric Rayleigh number $Ra_{ec} = 205$.

In 2014, Wang et al. designed an elaborate Y-type EK micromixer^{5, 25, 32} and demonstrated that micro electrokinetic (μ EK) turbulence could be generated under an alternating-current (AC) electric field with 100 kHz frequency. However, the additional control parameter, e.g. AC frequency, makes the comparison of working conditions with the previous reports unattainable. Further investigations by Nan et al.²¹ demonstrate that the conditions of inducing the most unstable mode of EK flow is inconsistent to that of generating highly-

developed EK turbulence. This further indicates the difficulty to advance a universal control parameter for EK turbulence, e.g. electric Rayleigh number (Ra_e). Although the Ra_e deduced from the Zhao-Wang model³³ can evaluate the flow status in a highly-developed AC EK turbulence, they are not appropriate indicators to show how the EK flow evolves from its initial status, which could be more crucial for engineering applications.

The strong diversity of dimensionless control parameters, e.g. Ra_e , could be attributed to the broad factors that influencing the electric body force in EK flow, including the form, intensity and frequency of electric field, the geometry of the flow field, the distribution of electric conductivity and permittivity, pH value, electrode property and etc. The entangled dynamics and interfacial phenomenon make the problem more complicated to reach a common sense on the format of Ra_e .

In this investigation, a novel Ra_e that describing the transition of AC EK flow of binary fluids from stable to unstable states is theoretically analyzed and experimentally evaluated in a divergent microchannel. We focus on how Ra_e is influenced by the physical and chemical conditions, e.g. electric field intensity, AC frequency, electric conductivity ratio and interface width. A theoretical analysis on electric Rayleigh number is conduct first. Then, the theory is adopted to predict the critical electric Rayleigh number Ra_{ec} of AC EK flow in a divergent microchannel. This study aims to show the newly developed electric Rayleigh number can better elucidate the underlying physics of how the electric body force perturbs the interface of the binary fluids. With the electric Rayleigh number, people can more precisely predict Ra_e , facilitating the comparison of physical and chemical conditions of generating EK flow. This is important for enhancing our understanding of the mechanisms of EK turbulence and promoting its application in microfluidics.

II. Theory and dimensionless parameters

A. Control equations

The EK flow can be described by Navier-Stokes equations as shown below^{34, 35}

$$\rho \left(\frac{\partial}{\partial t} \vec{u} + \vec{u} \cdot \nabla \vec{u} \right) = -\nabla p + \vec{F}_e + \mu \nabla^2 \vec{u} \quad (1)$$

$$\vec{F}_e = \rho_e \vec{E} - \frac{1}{2} (\vec{E} \cdot \vec{E}) \nabla \varepsilon + \frac{1}{2} \nabla \left[\rho \vec{E} \cdot \vec{E} \left(\frac{\partial \varepsilon}{\partial \rho} \right)_T \right] \quad (2)$$

$$\rho_e = \nabla \cdot \varepsilon \vec{E} \quad (3)$$

$$\frac{\partial}{\partial t} \sigma + \vec{u} \cdot \nabla \sigma = D_\sigma \nabla^2 \sigma \quad (4)$$

where ρ is fluid density, μ is dynamic viscosity, \vec{F}_e is electric body force (EBF). ε and σ are electric permittivity and electric conductivity of the solution respectively, while ρ_e is the charge density. The instantaneous velocity vector, $\vec{u} = u\vec{i} + v\vec{j} + w\vec{k}$, consist of u , v , w as the velocity components in streamwise, spanwise and vertical directions respectively, where \vec{i} , \vec{j} and \vec{k} are the unit vectors in these corresponding directions. D_σ stands for the diffusion coefficient. Furthermore, we also assume the fluid to be incompressible, i.e. $\nabla \cdot \vec{u} = 0$.

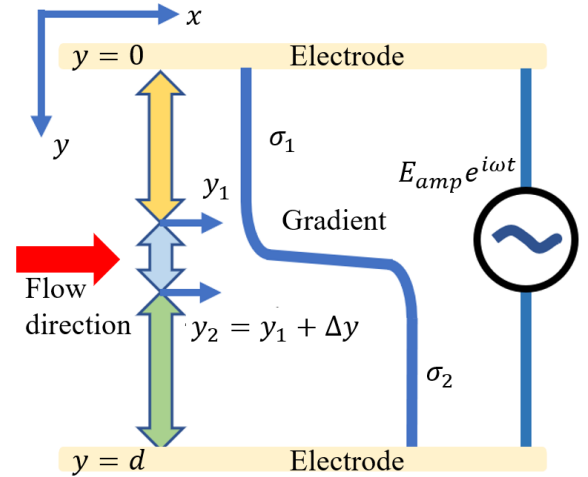


FIG. 1. Schematic diagram of electric conductivity distribution along y direction in initial stage. y_1 denotes the width with electric conductivity σ_1 . Δy represents the interface width with electric conductivity gradient. $d - y_2$ is the width with electric conductivity σ_2 . Note that, given the flow rate is the same, here $y_1 = d - y_2$.

In this model, we consider that the electric field is perpendicular to the interface of the binary fluids, as diagramed in Fig. 1, with the AC frequency (f_f) much higher than the response frequency (f_r) of the flow.³⁶ The fluids share identical viscosity, temperature and electric permittivity, yet differ in electric conductivity, denoted as σ_1 and σ_2 ($\sigma_2 \geq \sigma_1$).

Since the fluid is incompressible, $\frac{1}{2} \nabla \left[\rho \vec{E} \cdot \vec{E} \left(\frac{\partial \varepsilon}{\partial \rho} \right)_T \right] = 0$.

Accordingly, Eq. (2) becomes

$$\vec{F}_e = \rho_e \vec{E} - \frac{1}{2} (\vec{E} \cdot \vec{E}) \nabla \varepsilon \quad (5)$$

When an electric field is applied, initially, the interface between the binary fluids is slightly disturbed by the EBF. The

ultrasmall flow disturbance has three consequences. First, the distribution of electric conductivity has negligible difference from the case without EBF. Second, the convective transport of charge is much weaker than that of the electric field. Therefore, the charge conservation equation³⁷ becomes

$$\frac{\partial \rho_e}{\partial t} + \nabla \cdot \sigma \vec{E} = 0 \quad (6)$$

The third is that the disturbance of electric conductivity is negligible as well. Consequently, the electric field can be approximated as a 1D model in the y -direction, E_y . Thus, Eq. (6) can be rewritten in the following as

$$\frac{\partial}{\partial y} \sigma^* E_y = 0 \quad (7)$$

where $\sigma^* = i\omega\varepsilon + \sigma$ is the complex electric conductivity, with $\omega = 2\pi f_f$ denoting the angular frequency. So considering the complex Ohmic law, $\sigma^* E_y = J^*$, it is constant for y where J^* is complex electric current density.

B. Electric body force

In EK flow, EBF is the most important quantities that determines the state of flow, however, influenced by various factors. At the initial stage, the time-averaged AC EBF per unit volume can be rewritten as³⁴

$$\vec{F}_{e,ac} = \frac{1}{2} \mathcal{R}e \left[(\nabla \varepsilon \cdot \vec{E} + \varepsilon \nabla \cdot \vec{E}) \cdot \vec{E} - \frac{1}{2} E^2 \nabla \varepsilon \right]$$

where \vec{E} is the complex conjugation of electric field intensity and $\mathcal{R}e$ is the real part. We are unable to use a local $\vec{F}_{e,ac}$ to evaluate the influence of EBF on EK flow. To characterize the influence of EBF, especially aiding to engineering applications, a spatially averaged EBF³⁶ on the interface with a width of Δy is applied as

$$F_{e,\Delta y} = \langle F_{e,ac} \rangle_{\Delta y} = \frac{\varepsilon}{4\Delta y} \left| \frac{J^*}{\sigma^*} \right|^2 \Big|_{y_1}^{y_1+\Delta y} \quad (8)$$

where $\langle \cdot \rangle_{\Delta y}$ indicates the spatial averaging on Δy in the y direction. The complex current density is conserved in space as

$$J^* = \sigma_{\Delta y}^* E_{y,\Delta y} = \sigma_d^* E_{y,d} \quad (9)$$

where $\sigma_{\Delta y}^* = 1/\langle 1/\sigma^* \rangle_{\Delta y}$ and $E_{y,\Delta y} = \langle E_y \rangle_{\Delta y}$ are the complex electric conductivity and electric field intensity averaged on the interface with Δy respectively. Similarly, $\sigma_d^* = 1/\langle 1/\sigma^* \rangle_d$ and $E_{y,d} = E_{amp} e^{i\omega t}$ are the complex

electric conductivity and electric field intensity averaged across the channel width d respectively, where $E_{amp} = V_{amp}/d$ is the amplitude of the AC electric field and V_{amp} is the voltage amplitude between the two electrodes as shown in the Fig. 1. Thus, $|J^*|^2 = J^* \cdot J = \sigma_d \sigma_d^* E_{y,d} E_{y,d}^* = \sigma_d \sigma_d^* E_{amp}^2$. σ_d^* is strictly dependent on ω , ε and the spatial distribution of σ .

Here, we consider an initial case of the EK flow, where the EBF is too weak to induce a perturbation of σ . Thus, the distribution of σ can be approximated to be steady. Furthermore, we utilize a tanh distribution (Fig. 1) of electric conductivity to demonstrate how the EBF and the corresponding dimensionless parameters is influenced by the physical quantities. If the electric conductivity has a tanh distribution as below

$$\sigma(y) = \sigma_1 + \frac{e^{(2y-d)/y_s}}{e^{(2y-d)/y_s} + 1} (\sigma_2 - \sigma_1) \quad (10)$$

where y_s is a shape factor to characterize the distribution of σ . In the tanh model, to stimulate an interface width of Δy , approximately we have $y_s \approx \Delta y/10$. According to Eq. (10), σ_d^* can be calculated as

$$\sigma_d^* = \frac{1}{\langle \frac{1}{\sigma^*} \rangle_d} = \frac{2d\sigma_1^* \sigma_2^*}{y_s(\sigma_1 - \sigma_2) \ln \frac{\sigma_1^* + \sigma_2^* e^{d/y_s}}{\sigma_1^* + \sigma_2^* e^{-d/y_s}} + 2d\sigma_2^*} \quad (11)$$

Furthermore, according to $\sigma^* = \sigma + i\omega\varepsilon$ and Eq. (10), we have

$$\frac{1}{|\sigma^*|^2} \Big|_{y_1}^{y_1+\Delta y} = 16 \frac{(1 - \lambda^2) B_{\tanh}}{\sigma_1^2 A_{\tanh}} \quad (12)$$

where $\lambda = \sigma_2/\sigma_1$ is electric conductivity ratio, $\chi = 2\omega\varepsilon/(\sigma_1 + \sigma_2)$ is a dimensionless frequency, $m = \chi(1 + \lambda)$, $A_{\tanh} = [4(e^{\Delta y/y_s} \lambda + 1)^2 + m^2(e^{\Delta y/y_s} + 1)^2][4(e^{\Delta y/y_s} + \lambda)^2 + m^2(e^{\Delta y/y_s} + 1)^2]$ and $B_{\tanh} = (e^{2\Delta y/y_s} - 1)(e^{\Delta y/y_s} + 1)^2$. By substituting Eq. (12) into (8), with binomial expansion, we have

$$F_{e,\Delta y} = \frac{\varepsilon E_{amp}^2 B_{\tanh} (1 - \lambda^2) (4\lambda^2 + m^2) (4 + m^2)}{\Delta y A_{\tanh} C_{\tanh}} \quad (13)$$

where $C_{\tanh} = (1 - \lambda)^2 (y_s/d)^2 q_{\tanh} p_{\tanh} + (y_s/d)(1 - \lambda)(2\lambda - im) q_{\tanh} + (y_s/d)(1 - \lambda)(2\lambda + im) p_{\tanh} + 4\lambda^2 m^2$, with $q_{\tanh} = \ln \frac{2+im+(2\lambda+im)e^{d/y_s}}{2+im+(2\lambda+im)e^{-d/y_s}}$ and $p_{\tanh} =$

$$\ln \frac{2-im+(2\lambda-im)e^{d/y_s}}{2-im+(2\lambda-im)e^{-d/y_s}}$$

TABLE II. Comparison between the linear model and the tanh model.

	Linear model	Tanh model
Schematic diagram of electric conductivity distribution		
Electric conductivity distribution σ	$\begin{cases} \sigma_1, (0 \leq y < y_1) \\ \frac{\sigma_2 - \sigma_1}{\Delta y} (y - y_1) + \sigma_1, (y_1 \leq y < y_2) \\ \sigma_2, (y_2 \leq y \leq d) \end{cases}$	$\sigma_1 + \frac{e^{(2y-d)/y_s}}{e^{(2y-d)/y_s} + 1} (\sigma_2 - \sigma_1)$
$F_{e,\Delta y}$	$\frac{4\varepsilon E_{amp}^2 (1-\lambda)^2 (1-\lambda^2)}{\Delta y} A_{linear}$	$\frac{\varepsilon E_{amp}^2 B_{tanh} (1-\lambda^2) (4\lambda^2 + m^2) (4 + m^2)}{\Delta y} A_{tanh} C_{tanh}$
Ra_e	$\frac{4\varepsilon E_{amp}^2 \Delta y^2 (1-\lambda)^2 (1-\lambda^2)}{\rho \nu D_e} A_{linear}$	$\frac{\varepsilon E_{amp}^2 \Delta y^2 B_{tanh} (1-\lambda^2) (4\lambda^2 + m^2) (4 + m^2)}{\rho \nu D_e} A_{tanh} C_{tanh}$
	$A_{linear} = 4(1 - \Delta y/d)^2 (\lambda - 1)^2 (\lambda^2 + 2\lambda + 1 + m^2) + 2\Delta y/d (1 - \Delta y/d) (\lambda - 1) [2(q_{linear} + p_{linear}) + im(q_{linear} - p_{linear})] (m^2 + 2 + 2\lambda^2) + (\Delta y/d)^2 q_{linear} p_{linear} (16\lambda^2 + 4m^2 + 4m^2 \lambda^2 + m^4)$ $q_{linear} = \ln \frac{2\lambda + im}{2 + im}$ $p_{linear} = \ln \frac{2\lambda - im}{2 - im}$	$A_{tanh} = [4(e^{\Delta y/y_s} \lambda + 1)^2 + m^2 (e^{\Delta y/y_s} + 1)^2] [4(e^{\Delta y/y_s} + \lambda)^2 + m^2 (e^{\Delta y/y_s} + 1)^2]$ $B_{tanh} = (e^{2\Delta y/y_s} - 1) (e^{\Delta y/y_s} + 1)^2$ $C_{tanh} = (1 - \lambda)^2 (y_s/d)^2 q_{tanh} p_{tanh} + (y_s/d) (1 - \lambda) (2\lambda - im) q_{tanh} + (y_s/d) (1 - \lambda) (2\lambda + im) p_{tanh} + 4\lambda^2 m^2$ $q_{tanh} = \ln \frac{2 + im + (2\lambda + im)e^{d/y_s}}{2 + im + (2\lambda + im)e^{-d/y_s}}$ $p_{tanh} = \ln \frac{2 - im + (2\lambda - im)e^{d/y_s}}{2 - im + (2\lambda - im)e^{-d/y_s}}$

C. Electric Grashof number and electric Rayleigh number

The electric Grashof number and the electric Rayleigh number are two commonly used dimensionless parameters to describe the state of EK flow. The former represents the ratio of EBF relative to viscous force, while the latter further considers the influence of ion diffusion. According to Eq. (13),

the electric Grashof number³⁸ (Gr_e) can be quantified by

$$Gr_e = \frac{F_{e,\Delta y} \Delta y^3}{\rho \nu^2} = \frac{\varepsilon E_{amp}^2 \Delta y^2 B_{tanh} (1-\lambda^2) (4\lambda^2 + m^2) (4 + m^2)}{\rho \nu^2 A_{tanh} C_{tanh}} \quad (14)$$

The electric Rayleigh number (Ra_e) is further obtained according to $Ra_e = Gr_e Sc$, where $Sc = \nu/D_\sigma$ is Schmidt number. Then, we have

$$Ra_e = \frac{\varepsilon E_{amp}^2 \Delta y^2 B_{tanh} (1 - \lambda^2) (4\lambda^2 + m^2) (4 + m^2)}{\rho \nu D_e A_{tanh} C_{tanh}} \quad (15)$$

Ra_e in Eq. (15) is evaluated from the overall distribution of electric conductivity. It complexly interplays with λ , χ and the initial distribution (through y_1 , y_2 and Δy) of electric conductivity, in a relatively nonintuitive manner. This is apparently distant from the previous investigations (see Table I), where the electric Rayleigh number are simply evaluated through either simple local quantities or a linear distribution of control scalars. For comparison, a linear model for electric conductivity distribution is also advanced in this investigation, as summarized in Table. II.

II. Numerical calculation of Ra_e in both linear and tanh model

In this section, as indicated by Ra_e in the Table. II, we demonstrate how the following parameters, e.g. E_{amp} , Δy , λ and χ , contribute to the variations of Ra_e . Both the linear mode and tanh model are theoretically compared to reveal their difference on calculating Ra_e . To be consistent to experiments, some relevant parameters are given as: $d = 650 \mu\text{m}$, ε is 7.1×10^{-10} F/m, ρ is 10^3 kg/m^3 , ν is $10^{-6} \text{ m}^2/\text{s}$, $\sigma_1 + \sigma_2$ is $2.395 \times 10^{-1} \text{ S/m}$ and D_σ is $5 \times 10^{-10} \text{ m}^2/\text{s}$.

A. Electric conductivity ratio

First, the influence of λ on Ra_e in the initial stage of EK flow is analyzed, as shown in Fig. 2. Under the linear model, as depicted in Fig. 2(a), Ra_e increases rapidly and monotonically with increasing λ , eventually reaching a saturation point at $\lambda = O(10^2)$. This indicates a higher probability of reaching an unstable state at higher λ , accordingly, easier to get into a transition. There is no optimal λ related to the highest Ra_e in the linear model.

However, under the tanh model, Ra_e first increases with λ and then decreases at relatively smaller χ , as depicted in Fig. 2(b). This model provides us with the possibility of identifying an optimal λ to reach the highest Ra_e , for effectively perturbing flow and improving momentum and scalar transport. Relative to the linear model without optimal λ , the tanh model that predicts optimal λ can provide better consistency with previous experiments. For instance, Wang et al³⁸ found when the applied AC frequency was 100 kHz, i.e.

$\chi = 3.7 \times 10^{-3}$, an ultrafast EK mixing can be achieved with an optimal $\lambda = 5000$. Nan et al²¹ also observed different optimal λ for perturbing the electric conductivity interface under different χ .

From Fig. 2(b), it should be noted that only when $\chi \geq 3.7 \times 10^{-3}$ (i.e. $f_f = 100 \text{ kHz}$), Ra_e increases monotonically with λ . To avoid the violation of $\tau_{rex} \ll 1/\omega$ (where $\tau_{rex} = 1.7 \times 10^{-5}$ is the charge relaxation time)³⁶, a larger χ exceeding 3.7×10^{-2} is not applied in this study. In the range $1.1 \times 10^{-6} \ll \chi \ll 3.7 \times 10^{-2}$, we surprisingly find a special value of $\lambda_c \approx 200$ by the tanh model. When $\lambda \leq \lambda_c$, Ra_e is insensitive to χ .

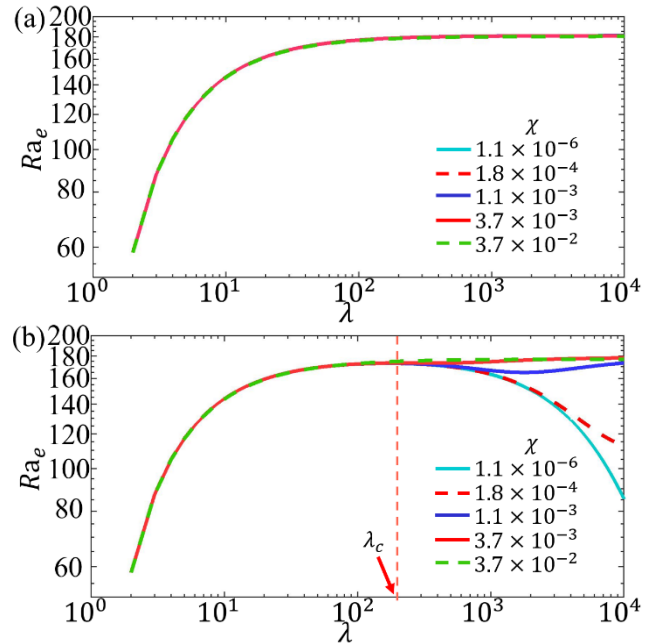


FIG. 2. Ra_e calculated from both linear and tanh models under different χ , where $d = 650 \mu\text{m}$, $\Delta y = \sqrt{4D_\sigma t} = 11.4 \mu\text{m}$ and $E_{amp} = 3.1 \times 10^4 \text{ V/m}$, where $t = x/U_e$ is the diffusion time of the interface. Here, U_e is the mean flow velocity at the centerline of the microchannel. $x = 0.2d$ is the measured position. All these data are consistent to the experimental conditions in the following. (a) Ra_e calculated by the linear model vs λ . (b) Ra_e calculated by the tanh model vs λ .

B. AC frequency

The insensitivity of Ra_e to χ at $\lambda \leq \lambda_c$ can be more visible in Fig. 3(b). All the plots at $\lambda \leq \lambda_c$ are exactly flat lines in the wide range of χ . However, when $\lambda > \lambda_c$, e.g. 2000 and 5400, Ra_e changes significantly with χ . It stays almost unchanged with χ first, then rapidly increases until reaching another plateau.

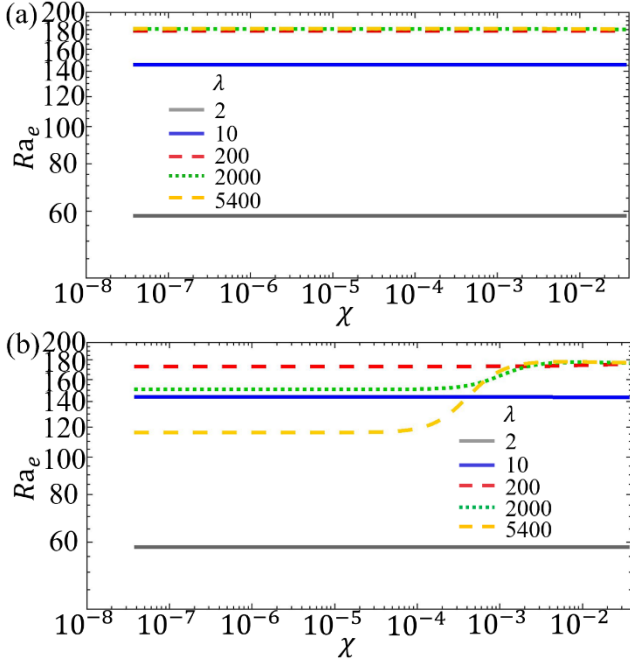


FIG. 3. Ra_e calculated from both linear and tanh models under different λ , where $d = 650 \mu\text{m}$, $\Delta y = 11.4 \mu\text{m}$ and $E_{amp} = 3.1 \times 10^4 \text{ V/m}$. (a) Ra_e calculated by the linear model vs χ . (b) Ra_e calculated by the tanh model vs χ .

In contrast, the variation of Ra_e with χ is not observed in Fig. 3(a), indicating the linear model has no capability to reveal the influence of χ (or AC frequency) on Ra_e . This accounts for why in previous experiments²¹, even though ultrafast EK mixing can be observed at $\chi > 3.7 \times 10^{-4}$ (or $f_f > 10 \text{ kHz}$), we still cannot get an apparently larger Ra_e through the linear model.

C. Interface width

As illustrated by a series of investigations^{21, 22, 38}, a larger gradient of electric conductivity is crucial for generating a larger EBF, accordingly a smaller Δy is preferred. Thus, a smaller Δy is corresponding to a larger Ra_e . For this purpose, we theoretically studied the effect of Δy on Ra_e . As depicted in Fig. 4, both models predict a larger Ra_e with increasing Δy as anticipated. The distinction lies in the fact that the tanh model can better distinguish the influence of Δy , as can be observed in Fig. 4(a, b).

D. Electric field intensity

In contrast to λ , χ and Δy which have complex relationship with Ra_e , the quadratic effect of electric field

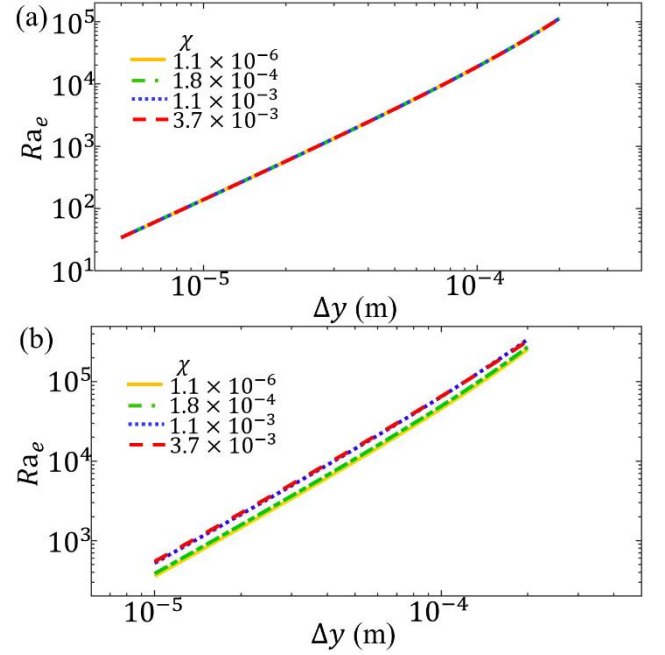


FIG. 4. Ra_e calculated from both linear and tanh models under different χ , where $d = 650 \mu\text{m}$, $\lambda = 5400$ and $E_{amp} = 3.1 \times 10^4 \text{ V/m}$. (a) Ra_e calculated by the linear model vs Δy . (b) Ra_e calculated by the tanh model vs Δy .

intensity is quite straightforward, i.e. $Ra_e \sim E_{amp}^2$ according to Eq. (15). This is also observable from Fig. 5(a, b). The difference between the linear and tanh model is that the latter is distinguishable for different χ , while the former is not.

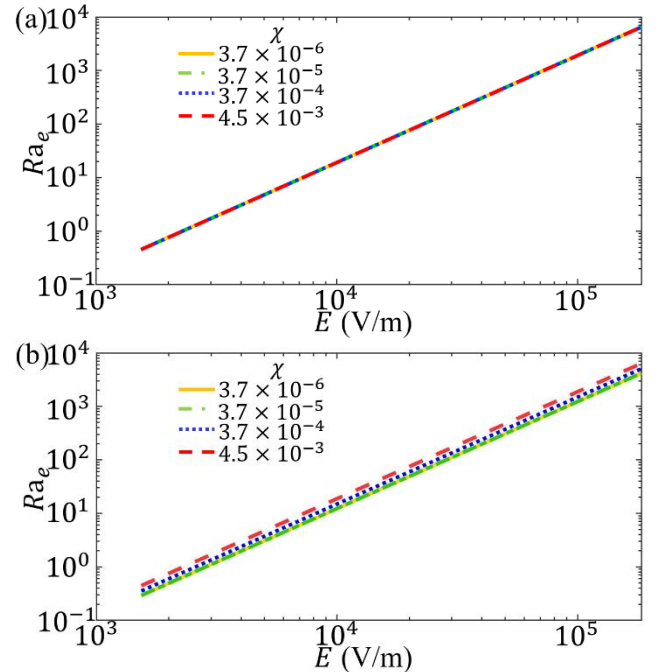


FIG. 5. Ra_e calculated from both linear and tanh models under different Δy , where $d = 650 \mu\text{m}$, $\chi = 3.7 \times 10^{-3}$ and $\lambda = 5400$. (a) Ra_e calculated by the linear model vs E . (b) Ra_e calculated by the tanh model vs E .

III. Experimental setup and results

A. Experimental setup

In this section, relying on the electric Rayleigh number Ra_e under the tanh model, we experimentally investigate the conditions when EK flow becomes unstable under AC electric field. To this end, the EK flow velocity is measured by laser induced fluorescence photobleaching anemometer (LIFPA), which has ultra-high spatial (~ 203 nm) and temporal (~ 4 μ s) resolution, as diagramed in Fig. 6(a). The system uses a 405nm continuous wave (CW) laser, with a laser power of 11 mW, as light source. An acousto-optic modulator (AOM) is applied to realize temporal control of the beam. The beam in turn passes through a special light filter (SLF) and a dichroic mirror (DM), and is then reflected into an objective lens (OL) to excite the fluorescent solution in the EK flow microchip. The fluorescent solution is Coumarin 102. The fluorescence emitted by the solution is filtered out by two bandpass filters

(BP, 470/100 and 470/10 nm), collected by an optical fiber (OF), measured by a photon counter (PT) and finally processed by a computer (PC).

The concentration of Coumarin102 solution is 100 μ mol/L. It is prepared by anhydrous ethanol and deionized water. Phosphate buffer solution (PBS) is applied to adjust the electric conductivity of the two solutions to reach $\lambda = 1:5400$, 1:2000, 1:200 and 1:2 respectively.

Fig. 6(b) illustrates the schematic diagram of the EK flow microchip. The microchannel is 100 μ m in high (h), 18 mm in long and 650 μ m in width between two electrodes. The two streams with different electric conductivity are injected separately from inlets 1 and 2 by a syringe pump. Consequently, a pronounced electrical conductivity gradient is established immediately following the trailing edge.

The measurement point (x_0 in Fig. 6(c)) is 150 μ m downstream of the trailing edge. x_1 serves as the velocity calibration location, which is about 2 mm downstream of the trailing edge. At this position, the pressure-driven basic flow

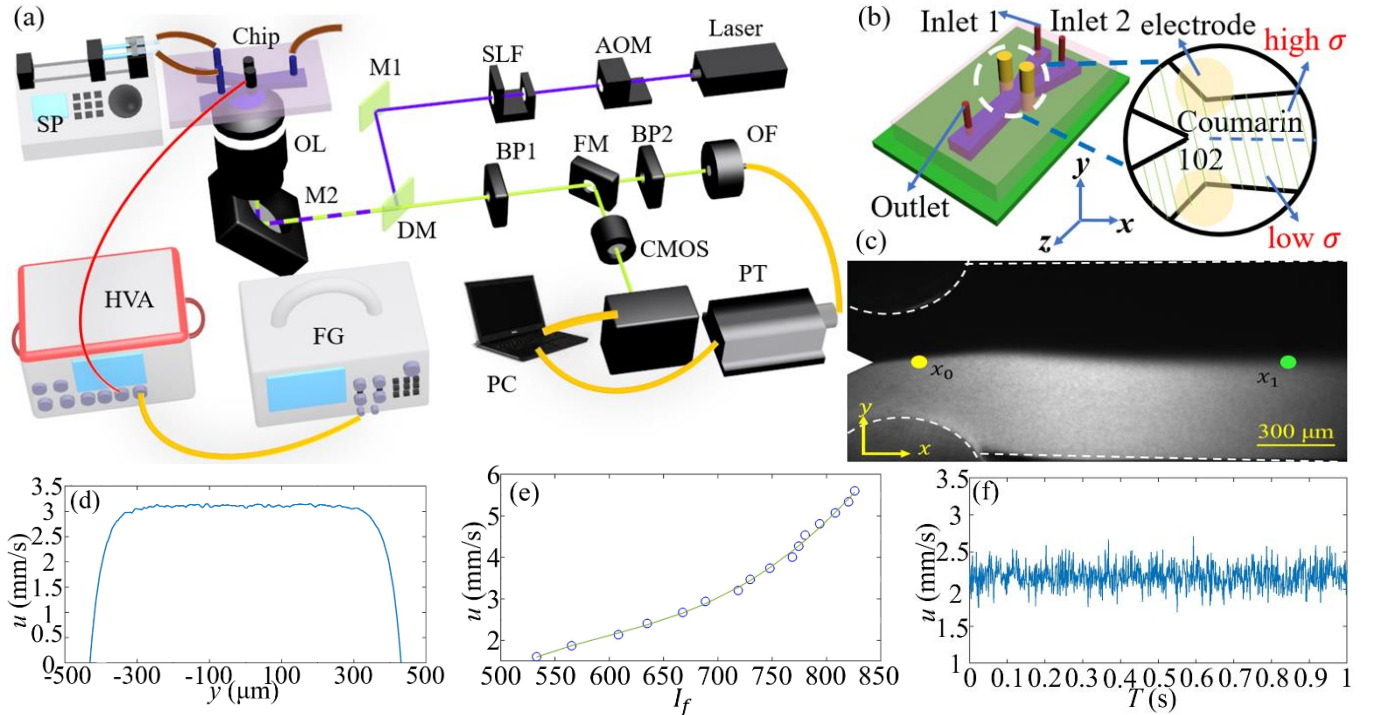


FIG. 6. Experimental system. (a) The diagram of LIFPA system. Laser: 405 nm continuous wave laser, AOM: Acousto-optic modulator, SLF: Spatial light filter, M1 and M2: mirrors, DM: Dichroic mirror, BP1 and BP2: Bandpass filters, FM: flipping mount mirror, OF: Photon counter, PT: Photon counter, PC: computer, FG: Function generator, HVA: High voltage amplifier, SP: Syringe pump, OL: Objective lens, CMOS: camera. (b) Structure diagram of the chip. (c) Flow visualization of the pressure-driven basic flow without electric field. x_0 is the measurement position. x_1 is the velocity calibration position. (d) The spanwise distribution of velocity in x_1 when $Q = 5$ μ L/min. (e) The velocity calibration in the center of channel. (f) The velocity time trace of $\chi = 1.8 \times 10^{-4}$, $\lambda = 5400$ and $\Delta y = 11.4$ μ m.

is stable and fully developed. The velocity profile at the velocity calibration point is numerically simulated by COMSOL Multiphysics, as shown in Fig. 6(d), to reveal the relationship between fluorescent intensity and velocity³⁹. A velocity calibration curve is plotted in Fig. 6(e). Fig. 6(f) shows a typical velocity time trace.

Through the analysis and comparison of the above two models, it is clear that the tanh model contains richer and more complex information about the influence of λ , χ and Δy on Ra_e . To demonstrate the effectiveness of the tanh model, we studied the critical electric Rayleigh number (Ra_{ec}), when the EK flow becomes unstable, under different control parameters. Ra_{ec} is determined from the power spectrum ($E(f)$) of the velocity fluctuations, as shown in Fig. 7(a). When no electric field was applied, a peak in $E(f)$, referred to as E_{peak} , is observed attributing to the perturbation of the wake after the trailing edge. When a smaller AC electric field was applied, i.e. $Ra_e < Ra_{ec}$, E_{peak} is equivalent to that observed without electric field. While AC electric field is over some threshold value, $Ra_e > Ra_{ec}$, E_{peak} increases rapidly with Ra_e , as plotted in Fig. 7(b), indicating an amplification of the flow perturbation induced by EBF. Through this way, Ra_{ec} can be determined (Fig. 7(b)).

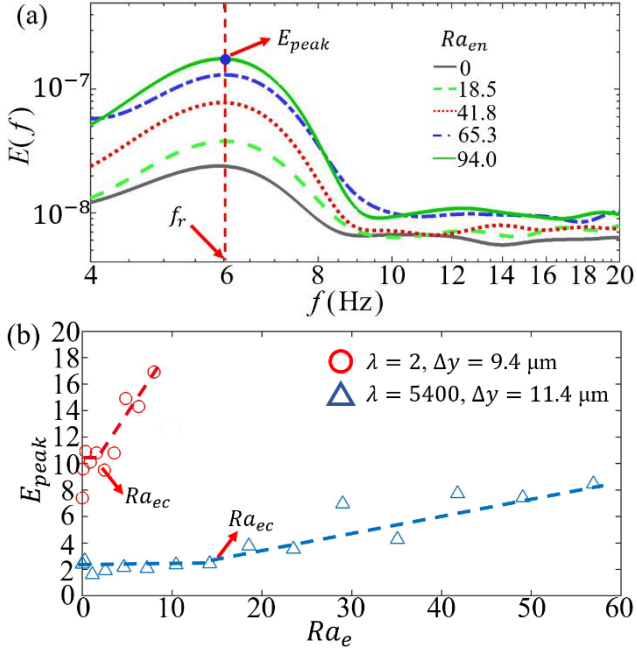


FIG. 7. Velocity power spectrum, E_{peak} and the determination of Ra_{ec} . (a) Velocity spectrum $E(f)$ at $\chi = 1.1 \times 10^{-6}$, $\lambda = 5400$ and $\Delta y = 11.4 \mu\text{m}$. (b) E_{peak} vs Ra_e showing the position of Ra_{ec} at $\chi = 1.1 \times 10^{-6}$.

B. Experimental results

The relevant experimental (the symbols) and theoretical (the dotted lines) results on Ra_{ec} are plotted in Figs. 8, 9 and 10 respectively. First, we analyze the influence of λ on Ra_{ec} , as plotted in Fig. 8. When $\chi = 1.1 \times 10^{-6}$, Ra_{ec} increases with λ first before subsequently decreasing in both experimental and theoretical results. Although the experimental one exhibits stronger bending relative to the theoretical one, their variation shows consistent trending. The consistency between experimental and theoretical results increases as χ increases, e.g. at $\chi = 1.8 \times 10^{-5}$. When $\chi = 3.7 \times 10^{-3}$, Ra_{ec} is monotonically increasing with λ . All the experimental trends align with the theoretical results predicted by the tanh model. In contrast, the most used model, i.e. linear distribution of σ , fails to provide even a qualitatively consistent prediction.

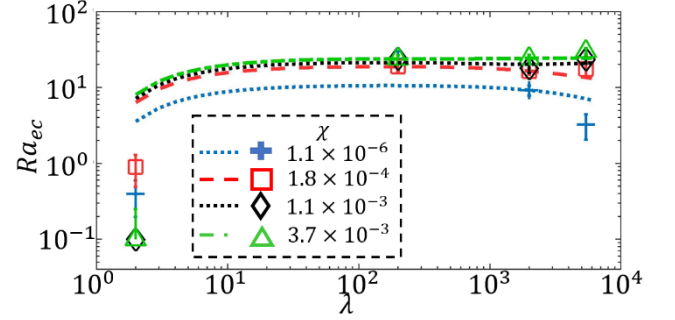


FIG. 8. Ra_{ec} vs λ under different χ with $\Delta y = 9.4 \mu\text{m}$.

Then, we further demonstrate the tanh model can effectively predict the influence of χ on Ra_{ec} . Both the experimental and theoretical results are plotted in Fig. 9. The experimental results indicate, when $\lambda \leq 200$, Ra_{ec} is almost unchanged with χ , which is consistent to the theoretical results. When $\lambda > 200$, the tanh model further reveals the complex variation of Ra_{ec} with χ , such that Ra_{ec} keeps constant first, then increases until reaching a plateau. The results again support the effectiveness of the tanh model.

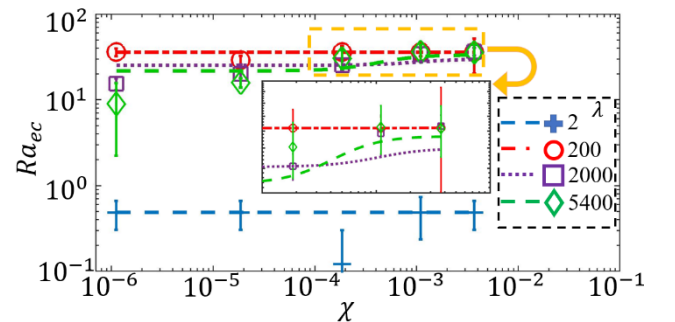


FIG. 9. Ra_{ec} vs χ under different λ with $\Delta y = 10.4 \mu\text{m}$.

The parameter Δy is crucial to the gradient of electric conductivity, which in turn, determines EBF and the corresponding electric Rayleigh number. From Fig. 10(a), the experimental results of Ra_{ec} are monotonically increasing with Δy , which is qualitatively consistent with the theoretical prediction by Eq. (15). Considering a larger Δy is corresponding to a smaller electric conductivity gradient and smaller EBF, it indicates that the flow is more difficult to be disturbed at a larger Δy under certain Reynolds number.

Finally, we also studied the influence of flow rate on Ra_{ec} , through bulk flow Reynolds number $Re = UL/\nu$, where $L = 2dh/(d+h)$ is the hydraulic diameter of the EK micromixers and U is the bulk flow velocity. From Fig. 10(b), it can be seen that Ra_{ec} has an inverse relationship with Re , indicating a decreasing requirement of AC electric field. Under a certain electric field, it is easier to generate unstable EK flow at a higher Re .

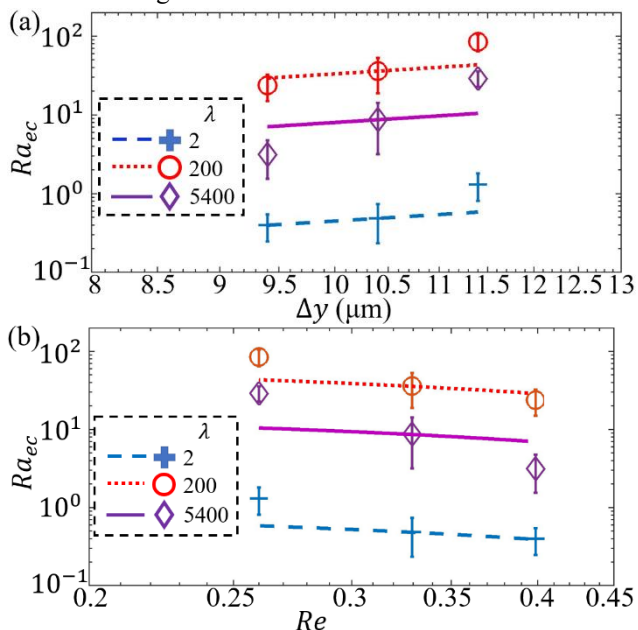


FIG. 10. (a) Ra_{ec} vs Δy under different λ with $\chi = 1.1 \times 10^{-6}$. (b) Ra_{ec} vs Re under different λ with $\chi = 1.1 \times 10^{-6}$.

IV. Discussion

Dimensionless parameters are vital for engineering applications where complex relations among multiple control parameters are interplayed. An effective dimensionless parameter that provides insight into the underlying relationship among the control parameters can also enhance our understanding of the complex physical mechanisms in an engineering system. Unfortunately, when more control

parameters are taken into account, it is significantly difficult to reach an effective dimensionless parameter. Part of the researchers believe that the pursuit of universal dimensionless parameter could be meaningless.

From this investigation, we aspire to show that, if a complex dimensionless parameter is appropriately expressed, it not only evaluates the status of the system, but also predicts (even though qualitatively) how the system changes. By using a more accurate distribution of electric conductivity, i.e. tanh model, the existence of optimal λ and χ can be predicted through the electric Rayleigh number. The AC EK flow in a divergent microchannel can be unstable with $Ra_{ec} = O(10^{-1})$. In contrast, the critical electric Rayleigh numbers in previous reports, e.g. Chen et al²³ and Nan et al²¹, are estimated to be 4.6×10^3 and 92.6 respectively, if using the tanh model in this investigation.

On the other hand, it should be noted that the current experimental and theoretical results, e.g. on the influence of Δy , still remain apparent discrepancies. This could be attributed to that the experimental environment is more complex relative to the theoretical model. Δy of the electric conductivity interface varies along streamwise, making the electric conductivity distribution in experiments intrinsically 2D or more. To change Δy , we change the flow rates of the two streams, which leads to the change of Re as well. It is almost impossible for us to isolate Δy and Re from each other in experiments. Thus, discrepancies become inevitable.

V. Conclusion

In this investigation, we theoretically derive the expression of electric Rayleigh number Ra_e for AC electrokinetic flow of binary fluids, on the basis of both linear and tanh distribution model of electric conductivity. The influence of electric conductivity ratio, AC frequency, interface width and electric field intensity on Ra_e is systematically investigated in the tanh model, and compared with the linear model. Through comparison, it can be found that the tanh model provides more information about the variation of Ra_e with the multiple parameters. In the tanh model, Ra_e is more sensitive to electric conductivity ratio, AC frequency and interface width.

Furthermore, we conduct an experimental investigation on the critical electric Rayleigh number of the EK flow evaluated by the tanh model, through velocity measurement

by LIFPA. The experimental findings exhibit an acceptable agreement with the theoretical predictions, thereby validating the efficacy of the electric Rayleigh number within the context of the tanh model.

An appropriate dimensionless parameter is not just a value, but an indicator of the underlying physical mechanism to guide engineering applications. In this paper, we propose a more accurate electric Rayleigh number to evaluate the state of AC EK flow, for designation of micromixers/reactors by electrokinetic approaches.

ACKNOWLEDGEMENTS

This research was funded by National Natural Science Foundation of China, grant number 51927804.

REFERENCES

- ¹K. Karthikeyan, S. K. Kandasamy, P. Saravanan and A. Alodhayb, "Numerical simulation and parameter optimization of micromixer device using fuzzy logic technique," *RSC Adv.* **13**, 4504-4522 (2023).
- ²D. S. Kim, S. H. Lee, C. H. Ahn, J. Y. Lee and T. H. Kwon, "Disposable integrated microfluidic biochip for blood typing by plastic microinjection moulding," *Lab Chip* **6**, 794-802 (2006).
- ³V. E. Papadopoulos, I. N. Kefala, G. Kaprou, G. Kokkoris, D. Moschou, G. Papadakis, E. Gizeli and A. Tserepi, "A passive micromixer for enzymatic digestion of DNA," *Microelectron. Eng.* **124**, 42-46 (2014).
- ⁴Z. Geng, S. L. Li, L. X. Zhu, Z. Cheng, M. Jin, B. X. Liu, Y. Guo and P. Liu, "Sample-to-Answer" Detection of Rare ctDNA Mutation from 2 mL Plasma with a Fully Integrated DNA Extraction and Digital Droplet PCR Microdevice for Liquid Biopsy," *Anal. Chem.* **92**, 7240-7248 (2020).
- ⁵S. S. Wang, Z. J. Li, S. Sheng, F. A. Wu and J. Wang, "Microfluidic biocatalysis enhances the esterification of caffeic acid and methanol under continuous-flow conditions," *J. Chem. Technol. Biotechnol.* **91**, 555-562 (2016).
- ⁶H. Z. Sun, Y. K. Ren, Y. Tao, T. Y. Jiang and H. Y. Jiang, "Three-Fluid Sequential Micromixing-Assisted Nanoparticle Synthesis Utilizing Alternating Current Electrothermal Flow," *Ind. Eng. Chem. Res.* **59**, 12514-12524 (2020).
- ⁷P. A. Auroux, D. Iossifidis, D. R. Reyes and A. Manz, "Micro total analysis systems. 2. Analytical standard operations and applications," *Anal. Chem.* **74**, 2637-2652 (2002).
- ⁸H. S. Santana, J. L. Silva, A. G. P. da Silva, A. C. Rodrigues, R. D. Amaral, D. Noriler and O. P. Taranto, "Development of a New Micromixer "Elis" for Fluid Mixing and Organic Reactions in Millidevices," *Ind. Eng. Chem. Res.* **60**, 9216-9230 (2021).
- ⁹C. Y. Lee and L. M. Fu, "Recent advances and applications of micromixers," *Sens. Actuator B-Chem.* **259**, 677-702 (2018).
- ¹⁰K. Illath, S. Kar, P. Gupta, A. Shinde, S. Wankhar, F. G. Tseng, K. T. Lim, M. Nagai and T. S. Santra, "Microfluidic nanomaterials: From synthesis to biomedical applications," *Biomaterials* **280**, 33 (2022).
- ¹¹G. Dutta, J. Rainbow, U. Zupancic, S. Papamatthaiou, P. Estrela and D. Moschou, "Microfluidic Devices for Label-Free DNA Detection," *Chemosensors* **6**, 20 (2018).
- ¹²X. Y. Chen and T. C. Li, "A novel passive micromixer designed by applying an optimization algorithm to the zigzag microchannel," *Chem. Eng. J.* **313**, 1406-1414 (2017).
- ¹³K. Karthikeyan, L. Sujatha and N. M. Sudharsan, "Numerical Modeling and Parametric Optimization of Micromixer for Low Diffusivity Fluids," *Int. J. Chem. React. Eng.* **16**, 11 (2018).
- ¹⁴M. Juraeva and D. J. Kang, "Mixing Enhancement of a Passive Micromixer with Submerged Structures," *Micromachines* **13**, 15 (2022).
- ¹⁵G. J. Liu, M. Wang, L. T. Dong, D. Y. Zhu, C. H. Wang, Y. H. Jia, X. B. Li and J. B. Wang, "A novel design for split-and-recombine micromixer with double-layer Y-shaped mixing units," *Sens. Actuator A-Phys.* **341**, 8 (2022).
- ¹⁶K. Karthikeyan and L. Sujatha, "Study of Permissible Flow Rate and Mixing Efficiency of the Micromixer Devices," *Int. J. Chem. React. Eng.* **17**, 15 (2019).
- ¹⁷A. D. Stroock, S. K. W. Dertinger, A. Ajdari, I. Mezic, H. A. Stone and G. M. Whitesides, "Chaotic mixer for microchannels," *Science* **295**, 647-651 (2002).
- ¹⁸H. Jalili, M. Raad and D. A. Fallah, "Numerical study on the mixing quality of an electroosmotic micromixer under periodic potential," *Proc. Inst. Mech. Eng. Part C-J. Eng. Mech. Eng. Sci.* **234**, 2113-2125 (2020).
- ¹⁹D. Bahrami, A. A. Nadooshan and M. Bayareh, "Numerical study on the effect of planar normal and Halbach magnet arrays on micromixing," *Int. J. Chem. React. Eng.* **18**, 11 (2020).

- ²⁰T. Dehghani, F. S. Moghanlou, M. Vajdi, M. S. Asl, M. Shokouhimehr and M. Mohammadi, "Mixing enhancement through a micromixer using topology optimization," *Chem. Eng. Res. Des.* **161**, 187-196 (2020).
- ²¹K. Y. Nan, Y. X. Shi, T. Y. Zhao, X. W. Tang, Y. Q. Zhu, K. G. Wang, J. T. Bai and W. Zhao, "Mixing and Flow Transition in an Optimized Electrokinetic Turbulent Micromixer," *Anal. Chem.* **94**, 12231-12239 (2022).
- ²²J. C. Baygents and F. Baldessari, "Electrohydrodynamic instability in a thin fluid layer with an electrical conductivity gradient," *Physics of Fluids* **10**, 301-311 (1998).
- ²³C. H. Chen, H. Lin, S. K. Lele and J. G. Santiago, "Convective and absolute electrokinetic instability with conductivity gradients," *Journal of Fluid Mechanics* **524**, 263-303 (2005).
- ²⁴J. D. Posner and J. G. Santiago, "Convective instability of electrokinetic flows in a cross-shaped microchannel," *J. Fluid Mech.* **555**, 1-42 (2006).
- ²⁵G. R. Wang, F. Yang and W. Zhao, "There can be turbulence in microfluidics at low Reynolds number," *Lab Chip* **14**, 1452-1458 (2014).
- ²⁶J. Wu, P. Traoré, A. T. Pérez and M. Zhang, "Numerical analysis of the subcritical feature of electro-thermo-convection in a plane layer of dielectric liquid," *Physica D: Nonlinear Phenomena* **311-312**, 45-57 (2015).
- ²⁷Yoshikawa, H., N., Crumeyrolle, O., Meyer, A., Mutabazi and I., "Linear stability of a circular Couette flow under a radial thermoelectric body force," *Physical review, E. Statistical, nonlinear, and soft matter physics* **91**, (2015).
- ²⁸W. Hassen, L. Kolsi, H. A. Mohammed, K. Ghachem, M. Sheikholeslami and M. A. Almeshaal, "Transient electrohydrodynamic convective flow and heat transfer of MWCNT - Dielectric nanofluid in a heated enclosure," *Physics Letters A* **384**, (2020).
- ²⁹M. H. Oddy, J. G. Santiago and J. C. Mikkelsen, "Electrokinetic instability micromixing," *Anal. Chem.* **73**, 5822-5832 (2001).
- ³⁰H. Lin, B. D. Storey, M. H. Oddy, C.-H. Chen and J. G. Santiago, "Instability of electrokinetic microchannel flows with conductivity gradients," *Physics of Fluids* **16**, 1922-1935 (2004).
- ³¹J. D. Posner and J. G. Santiago, "Convective instability of electrokinetic flows in a cross-shaped microchannel," *Journal of Fluid Mechanics* **555**, (2006).
- ³²G. R. Wang, F. Yang, W. Zhao and C. P. Chen, "On micro-electrokinetic scalar turbulence in microfluidics at a low Reynolds number," *Lab Chip* **16**, 1030-1038 (2016).
- ³³W. Zhao and G. R. Wang, "Scaling of velocity and scalar structure functions in ac electrokinetic turbulence," *Phys. Rev. E* **95**, 12 (2017).
- ³⁴A. Ramos, H. Morgan, N. G. Green and A. Castellanos, "AC Electrokinetics: A Review of Forces in Microelectrode Structures," *Journal of Physics D Applied Physics* **31**, 2338-2353 (1998).
- ³⁵Z. Y. Hu, T. Y. Zhao, W. Zhao, F. Yang, H. X. Wang, K. G. Wang, J. T. Bai and G. R. Wang, "Transition from periodic to chaotic AC electroosmotic flows near electric double layer," *Aiche J.* **67**, 12 (2021).
- ³⁶W. Zhao and G. Wang, "Scaling of velocity and scalar structure functions in ac electrokinetic turbulence," *Phys Rev E* **95**, 023111 (2017).
- ³⁷A. Ramos, H. Morgan, N. G. Green and A. Castellanos, "Ac electrokinetics: a review of forces in microelectrode structures," *Journal of Physics D: Applied Physics* **31**, 2338-2353 (1998).
- ³⁸G. R. Wang, F. Yang and W. Zhao, "There can be turbulence in microfluidics at low Reynolds number," *Lab Chip* **14**, 1452-1458 (2014).
- ³⁹W. Zhao, F. Yang, J. Khan, K. Reifsnider and G. R. Wang, "Measurement of velocity fluctuations in microfluidics with simultaneously ultrahigh spatial and temporal resolution," *Exp. Fluids* **57**, 12 (2016).